ACS Energy LETTERS

http://pubs.acs.org/journal/aelccp

Letter

Chemical and Structural Insights into Solid Electrolyte Interphase Evolution for Sodium Metal Electrodes

Chang-An Lo, Aditya Singla, Varun R. Kankanallu, Dean Yen, Bairav S. Vishnugopi, Eliot Gann, Lutz Wiegart, Partha P. Mukherjee,* Cherno Jaye, Patryk Wąsik, and Yu-chen Karen Chen-Wiegart*

Cite This: *ACS Energy Lett.* 2026, 11, 3181−3189

Read Online

ACCESS | Metrics & More | Article Recommendations | Supporting Information

ABSTRACT: The solid electrolyte interphase (SEI) critically governs the reversibility of sodium metal batteries, through dynamically mediating ion transport and interfacial reactions. However, its kinetic evolution under operating conditions, and how it influences interfacial stability, remains poorly understood. Here, we reveal that the SEI undergoes coupled chemical and mechanical changes during sodium plating and stripping, leading to spatial and temporal heterogeneity that drives interfacial degradation. Synchrotron *operando* grazing-incidence wide-angle X-ray scattering and soft X-ray absorption spectroscopy capture the sequential formation and dissolution of inorganic SEI phases (NaF, NaH, NaOH, Na_2PO_3F), accompanied by depth-dependent alterations in organic SEI components. Mesoscale modeling connects this evolving SEI heterogeneity to localized current density fluctuations and stress accumulation at the Na interface, identifying pathways to electrically isolated sodium formation. These findings show that SEI instability fundamentally limits reversibility in sodium metal batteries, and that controlling SEI chemistry−mechanics coupling is essential to achieving its durability.

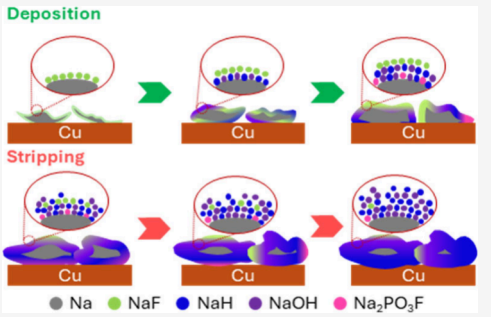

Lithium-ion batteries (LIBs) have transformed the landscape of modern energy storage, powering applications ranging from portable electronics to electric vehicles and renewable energy systems.[1] However, the rapid increase in global demand has heightened concerns about the sustainability of lithium resources, which are both limited and geographically concentrated.[2] To address it, sodium-based battery technologies—particularly sodium-ion batteries (SIBs) and sodium metal batteries (SMBs)—have emerged as promising alternatives.[3] Among them, SMBs offer significant theoretical and practical advantages, such as the high specific capacity (1165 mAh g^{-1}) and low redox potential (330 mV vs. Li/Li^+) of sodium metal.[4] These properties position SMBs as promising candidates for large-scale, cost-effective, and energy-dense storage. However, the commercialization of SMBs is challenged by existing issues at the electrode−electrolyte interface: the formation of unstable solid-electrolyte interphase (SEI) layers and the growth of Na dendrites.[5] These interfacial instabilities are mutually reinforcing: an inhomogeneous or fragile SEI promotes uneven Na^+ flux and dendritic growth, which in turn damages the SEI and initiates additional parasitic reactions.[5,6]

SEI, a passivation layer formed via the reductive decomposition of electrolyte components at the metal surface, is essential for regulating ion transport and suppressing continuous side reactions. Tremendous research has been focused on improving SEI stability through electrolyte engineering,[7−9] such as employing ether-based solvents,[10] fluorinated additives,[11,12] or sodiophilic artificial interphases,[13,14] to encourage uniform Na deposition and mitigate dendrite formation.

Despite its importance, characterizing the SEI remains highly challenging. The layer is chemically complex, nanoscale thin, and buried beneath the electrolyte, making it difficult to observe directly, especially in *operando* conditions.[15,16] While techniques such as X-ray photoelectron spectroscopy (XPS),[10] nuclear magnetic resonance (NMR),[17,18] cryo-electron microscopy, and electrochemical quartz crystal microbalance (EQCM) have provided insights into SEI chemistry in lithium systems, their application to Na metal interfaces has been scarce.[19,20] Meanwhile, although significant research effort has been made in understanding Na plating behavior, the stripping process remains less studied. One particularly detrimental failure mode that arises during stripping is the formation of "dead Na"—electrically disconnected sodium deposits that no longer participate in cycling, leading to capacity loss and lower Coulombic efficiency.[21] Fully understanding the coupled evolution of SEI and Na metal morphology during both plating and stripping is therefore critical for achieving durable and reversible SMB operation.

Received: October 27, 2025
Revised: February 19, 2026
Accepted: February 26, 2026
Published: March 5, 2026

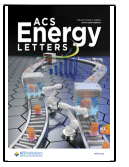

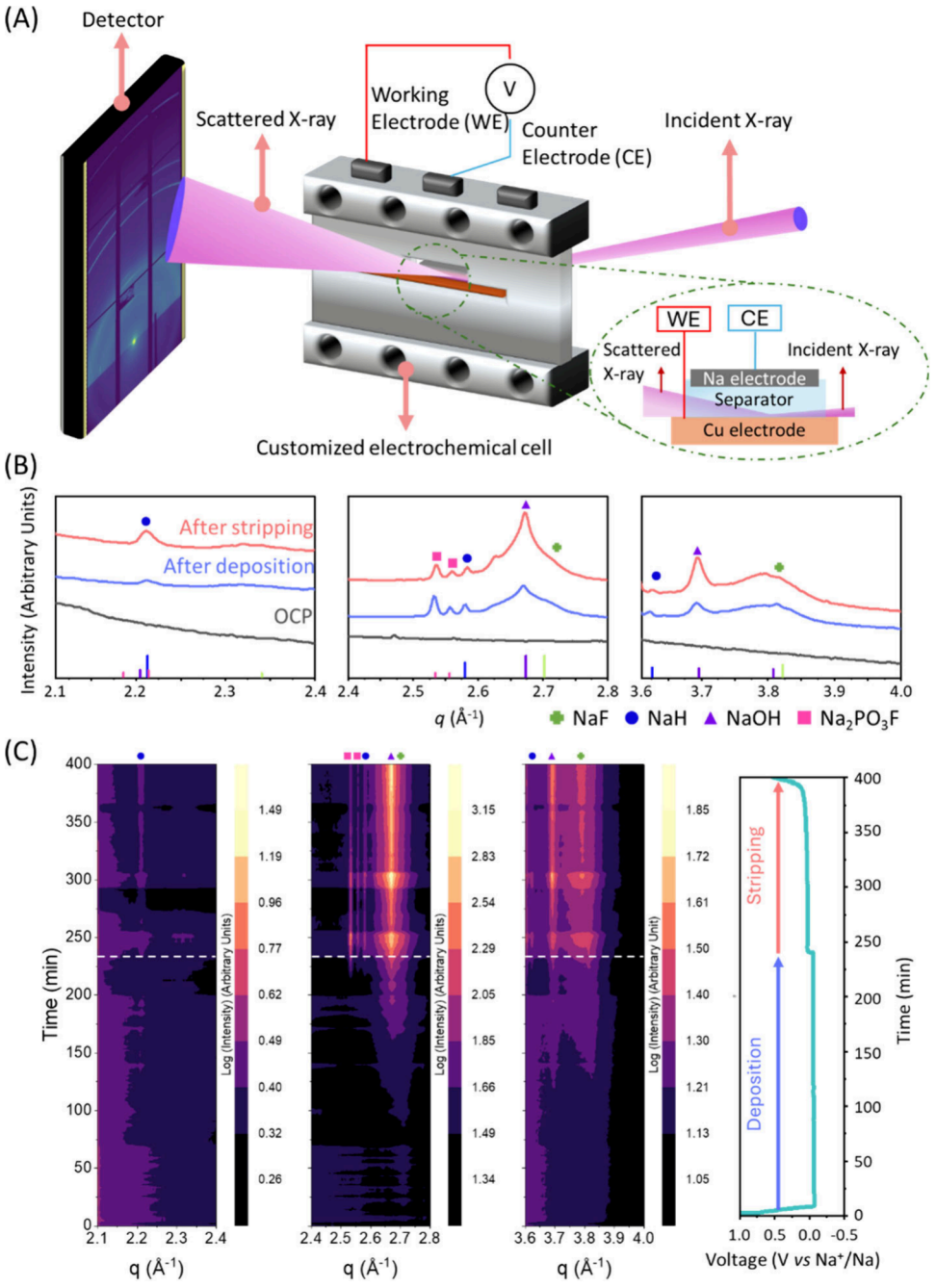

Figure 1. (A) *Operando* 2D GIWAXS setup at the SMI beamline of NSLS-II at BNL and (B) the representative indexed GIWAXS patterns for open-circuit potential (OCP), after deposition and stripping within selected q-ranges. Indexed GIWXAS patterns with entire a wider q-range are shown in the Supporting Information. (C) Time-dependent GIWAXS heatmaps in logarithm scale along with corresponding voltage profiles. The data reveal the sequential formation and dissolution of SEI phases such as NaF, NaH, NaOH, and Na_2PO_3F during cycling.

Our recent work demonstrates that grazing-incidence wide-angle X-ray scattering (GIWAXS) can be used to study SEI of Na metal anode.[22] However, the SEI is not a static structure but continuously evolves during electrochemical cycling. While *ex-situ* techniques have provided valuable insights in resolving SEI species as a function of electrochemical conditions and substrate interfaces, they are inherently limited in capturing the real-time evolution of SEI under operating conditions. To overcome these barriers, *operando* characterization approaches are essential. In this work, *operando* GIWAXS and soft X-ray absorption spectroscopy (sXAS) were performed to gain complementary structural and chemical insights into the evolution of SEI for Na electrodeposition/stripping. *Operando* GIWAXS enables real-time studies of the nucleation, growth, and transformation of crystalline SEI species under electrochemical cycling for Na metal anode for the first time. This reveals time-resolved changes in crystallographic texture and preferred orientation, highlighting different-staged growth behavior in various SEI species such as NaH and NaF. To complement the GIWAXS technique that focuses on crystalline inorganic phases, in parallel, sXAS in total and partial electron yield modes captures the depth-dependent chemical composition of the SEI, including both crystalline and amorphous species, as well as distinguishing inorganic

https://doi.org/10.1021/acsenergylett.5c03538
ACS Energy Lett. 2026, 11, 3181−3189

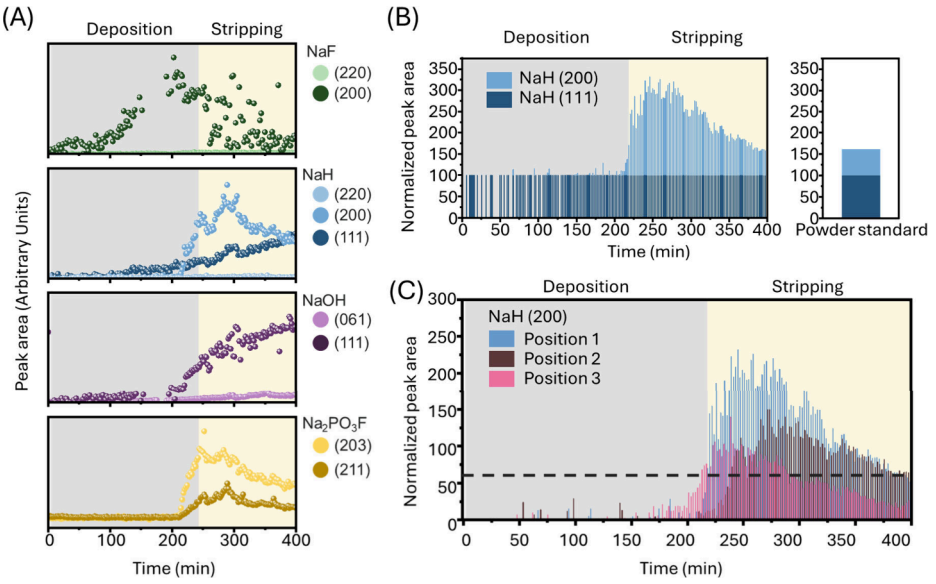

Figure 2. SEI characterization using *operando* GIWAXS. (A) Evolution of the integrated peak areas for various SEI species (NaF, NaH, NaOH, and Na_2PO_3F) during Na electrodeposition (gray-shaded region) and stripping (yellow-shaded region). A zoom-in view of the NaF (220) and NaH (220) peaks is provided in Figure S3. (B) Investigation of preferred orientation in NaH through scaled diffraction peak areas of NaH (111) and (200) as a function of reaction time. The data are compared with the isotropic powder standard (PDF# 04-018-2335). (C) Heterogeneity of NaH (200) evolution across three different sample positions with each position spaced 50 μm apart. The bar charts show scaled NaH diffraction peak areas for NaH (111) and NaH (200) intensity vs. reaction time. The dashed line corresponds to the normalized peak area of the powder standard listed above.

species in the outer layers from evolving organic components deeper within. Together, these techniques uncover a progressive enrichment of carbonate/hydroxide in outer SEI layer during cycling. The multimodal synchrotron X-ray characterization approach offers a mechanistic understanding of SEI formation, passivation, and degradation. More importantly, we augment these experimental observations with mesoscale modeling that simulates the dynamic interplay between electrochemical reactions, interfacial mechanics, and SEI morphology. The model captures spatial−temporal evolution, heterogeneity, and instability that lead to isolated sodium and incomplete passivation, connecting to the degradation in performance. Together, the *operando*, multimodal analysis and mesoscale modeling approach advances the fundamental understanding of SEI evolution in Na metal batteries and informs strategies to enhance anode durability.

To track the evolution of the SEI during Na electrodeposition/stripping, *operando* GIWAXS measurements were performed on a Na−Cu half-cell using a customized electrochemical cell, as shown in Figure 1(A). Figure S1 provides details of the probing-depth analysis as a function of the incident X-ray angles, along with the associated discussion. Figure 1(B) presents representative indexed GIWAXS patterns with selected q-range and various SEI species, including NaH, Na_2PO_3F, NaOH, and NaF are identified. These SEI species are consistent with previous studies[12,23]

The inorganic SEI layer plays a critical role in determining the cyclability of sodium metal anodes. Studies have shown that an SEI with a Young's modulus around 5.2 GPa (approximately 1.8 times that of sodium metal) can effectively suppress sodium dendrite growth.[18,24] Notably, NaH has been reported to possess a higher Young's modulus (approximately 45 GPa), far exceeding this threshold, which may contribute to improved cycling stability.[24] In addition, the electronically insulating nature of NaH helps to minimize further electrolyte decomposition, further enhancing the durability of the SEI.[18,25] Figure 1(C) highlights the time-dependent GIWAXS heatmaps along with corresponding voltage profiles across different q-ranges, revealing sequential formation and dissolution of SEI phases as a function of electrochemical cycling. Figure S2 shows the GIWAXS heatmap for the entire q-range as collected during the experiment. These *operando* observations demonstrate that the SEI is not static but dynamically evolves under electrochemical cycling, with multiple species contributing to its transient nature.

To better visualize peaks evolution of various SEI species, Figure 2(A) and Figure S3 present the evolution of the area under the curves for NaF, NaH, NaOH and Na_2PO_3F during Na electrodeposition and stripping. In electrodeposition, Figure 2(A) shows NaF (200) and (220) appear early and consistently, suggesting NaF is a primary, rapidly forming, and relatively stable SEI component.[10] In contrast, NaH (111) and (200) emerge later, predominantly during the latter part of deposition. NaOH (111) and (061) increase gradually during plating and persist during stripping, consistent with its continued accumulation. Na_2PO_3F (203) and (211) crystallize during late stages of plating, implying they are products likely formed from salt decomposition.[26] The distinct onset times and growth rates across SEI phases suggest differing kinetic pathways.

In stripping, Figure 2(A) shows different SEI species exhibit distinct behaviors. For fluorine-derived SEI species, the significant change of NaF indicates its transient nature, suggesting that NaF is not a static component in SEI, but rather a dynamic and evolving compound that undergoes intermittent formation, cracking or dissolving.[27,28] Fluorine-containing SEI components, such as NaF and Na_2PO_3F, are widely considered to enhance passivation due to their high Young's modulus, providing mechanical robustness to prevent Na metal from contacting the electrolyte.[29,30] Therefore, the

https://doi.org/10.1021/acsenergylett.5c03538
ACS Energy Lett. 2026, 11, 3181−3189

decreasing intensity of Na_2PO_3F (203) and (211) during stripping indicates partial dissolution of Na_2PO_3F within the SEI, suggesting a disruption of the passivation layer. As the passivation layer breaks down, fresh Na is exposed to the electrolyte, triggering additional side reactions.[31] This phenomenon likely accounts for the continued increase in NaH and NaOH intensity during Na stripping.

Notably, NaH also exhibits a distinct preferred orientation behavior during cycling. Figure 2(B) shows orientation intensity profiles — compared with the randomly orientated X-ray diffraction standard (PDF# 04-018−2335) — reveal a strong [111] texture throughout most of the plating period. However, the [200] orientation becomes increasingly prominent at the onset of stripping, with the strongest textural anisotropy observed approximately 10 min into the stripping process. After extended stripping time, the (200)/(111) intensity ratio approaches that of the powder diffraction standard, also shown in Figure 2(B), which indicates that the preferred orientation was diminishing. This observed trend indicates a change in the average orientation of NaH crystallites during cycling. At the initial stage of deposition, the NaH (111) diffraction peak is strongest, suggesting that most newly formed NaH grains have their (111) planes preferentially aligned parallel to the substrate. As deposition continues and the crystals grow, the (200) peak becomes more prominent, indicating that larger or newly formed grains increasingly exhibit (200) orientation as well. This evolution in the (111)/(200) intensity ratio shows the dynamic nature of NaH growth, where the overall orientation distribution becomes more diverse. The decrease in texture during stripping likely results from partial dissolution or the formation of new, less aligned NaH crystallites, leading to a more random orientation distribution. Although the NaH orientation appears to change during stripping, this does not imply reorientation of existing crystallites. Instead, the data suggest that NaH (111) plane formed during plating partially dissolves during stripping, and newly formed NaH nucleates with a different preferred orientation, predominantly (200). This orientation shift is likely triggered and influenced by changes in local interfacial conditions during stripping, including uneven SEI breakdown, heterogeneous electrolyte access, and local variations in Na surface morphology or stress fields. Such factors can modify nucleation energetics and promote different crystallographic orientations for newly formed NaH.

Not only does chemical species distribution affect Na plating/stripping, but the spatial heterogeneity of SEI is also a critical factor. To probe spatial heterogeneity, Figure S4 compares SEI formation across two different sample positions. NaF consistently appears as the first SEI compound to form and is also the first to disappear during stripping, suggesting that it may not provide sustained protection for the Na metal surface. Ideally, once the SEI is formed, it should act as a stable, passivating film that prevents additional electrolyte from reaching the underlying Na deposits, thus inhibiting further side reactions and continuous SEI growth. The disappearance of NaF during cycling implies that the SEI may not be fully effective in blocking electrolyte access, allowing continued contact and reaction between Na metal and the electrolyte. This may explain the continued accumulation of NaOH during the stripping.

The role of NaH in sodium electrodeposition/stripping remains a subject of ongoing debate. Some studies suggest that NaH is detrimental, arguing that its wide-bandgap insulating nature can electrically isolate sodium metal, leading to the formation of dead Na and reduced capacity.[32] Conversely, other researchers propose that NaH could serve as a beneficial SEI component, as its insulating properties may protect the sodium metal from direct contact with the electrolyte, thereby suppressing side reactions.[18,25] As a result, a comprehensive understanding of NaH formation and evolution is essential for advancing sodium metal battery technology.

NaH exhibits a more complex spatial-temporal distribution, coupled with changes in its preferred crystallographic orientation. Figure S5 shows the normalized intensities of NaH (111) and (200) at two additional, different sample positions. For reference, the intensity of NaH (200) normalized to NaH (111), in the powder standard is 61.3 as shown in Figure 2 (B). To directly compare the heterogeneity, Figure 2(C) shows the NaH (200) scaled intensities extracted from Figure 2(B) and Figure S5 as a function of reaction time. The dashed line in the figure indicates the intensity level of the powder standard. During electrodeposition, Figure S5 shows a predominant signal from NaH (111) across the sample, suggesting NaH shows similar texture. However, upon the stripping, textural heterogeneity emerges with pronounced variations in crystallographic orientation across different sample positions. This indicates localized structural changes, likely driven by uneven interfacial stresses, current density, dissolution rates, or electrolyte access. Such spatial variability suggests that the stripping process is not uniform across the electrode, potentially governed by local differences in Na morphology, SEI breakdown, or electric field distribution. Furthermore, the local differences established during the first cycle are expected to influence subsequent electrodeposition and stripping behavior. Figure S6 presents the *operando* GIWAXS results for the second cycle and further analysis (Figure S7). Because the first cycle was performed in the laboratory before the cell was transferred to the beamline, some SEI phases—such as NaF and NaH—partially dissolved or transformed, and therefore are not visible at the beginning of the second-cycle GIWAXS measurement. During the second plating/stripping sequence, NaF (200) and NaOH (111) again display similar behavior: both reform during electrodeposition and disappear during stripping. In contrast, Na_2PO_3F remains relatively stable throughout the entire cycle, showing minimal change in intensity. Importantly, the spatial variation becomes more pronounced in the second cycle. Figure S8−9 show that different sample positions exhibit noticeably different SEI evolution pathways, indicating that the heterogeneity observed in the first cycle becomes even more severe in the subsequent cycle.

In addition to the *operando* measurements, Figure S10 presents *ex-situ* GIWAXS data for the second cycle as a complementary measurement, revealing distinct evolution pathways for NaH and NaF. NaH exhibits clear orientation changes between deposition and stripping: during deposition, NaH forms predominantly with a strong (111) texture, while during stripping, the (111) reflection diminishes and newly formed NaH displays a pronounced (200) orientation. This behavior indicates that NaH is not simply retained throughout cycling but is continuously dissolved and reformed with different crystallographic preferences depending on the local interfacial environment. In contrast, NaF behaves more transiently—its (200) reflection is prominent during deposition but largely disappears after stripping, demonstrating that NaF readily dissolves or reacts once Na is stripped. These *ex-*

https://doi.org/10.1021/acsenergylett.5c03538
ACS Energy Lett. 2026, 11, 3181−3189

situ findings reinforce the *operando* observations, demonstrating that NaH reforms with cycle-dependent preferred orientations, whereas NaF remains a highly reversible SEI component that dissolves once sodium is removed.

To further elucidate the role of NaH, Figure S11 shows incidence-angle-resolved GIWAXS patterns performed on cycled Na anodes. By tuning the incidence angle, we access different probing depths, allowing us to track how NaH evolves both near the surface and deeper within the SEI. Figure S12 presents the normalized peak areas of the NaH (111) and (200) reflections at different probing depths, revealing clear depth-dependent variations in preferred orientation. During the first deposition, NaH near the surface (low incidence angle) predominantly exhibits the (111) orientation, whereas deeper regions show an increasing contribution from the (200) reflection, indicating that NaH nucleates and grows with different crystallographic preferences as the deposition occurs. During stripping, this trend reverses. The surface region becomes enriched in newly formed NaH with stronger (200) character, while residual NaH (111) remains detectable at greater depths. These results demonstrate that NaH does not form uniformly but instead develops distinct, depth-dependent crystallographic orientations that evolve with the electrochemical stage, supporting the view that NaH undergoes continuous dissolution and reformation with orientation preferences governed by the local interfacial environment.

Our results provide insight into the two debated interpretations of NaH in sodium metal anodes, as NaH can act either as an insulating phase that isolates sodium or as a protective component that enhances sodium passivation. The strong and persistent crystallographic texture of NaH during deposition suggests that it can form an ordered, mechanically stiff interphase, consistent with the view that NaH contributes to passivation and surface stabilization. However, the dissolution and reformation of NaH during stripping indicate that it does not uniformly cover the interface; such heterogeneous domains may locally block Na transport and effectively isolate metallic Na. Thus, NaH can simultaneously exhibit protective behavior where it is continuous and insulating behavior where it forms patchy domains. The observed depth- and stage-dependent evolution supports a dual role, with the net effect determined by how uniformly NaH forms and whether its preferred orientation enables or impedes Na^+ flux. Overall, NaH is insulating in all directions though, its impact on Na^+ transport depends strongly on how it forms. During deposition, NaH(111) grows as a thin, surface-parallel layer, making it less impeded to interfacial Na ion flux. In contrast, the NaH(200) formed during stripping appears in more localized and nonuniform domains, which can create ion-blocking regions and hinder uniform Na deposition and stripping.

In terms of Na texture, both the deposited Na and the residual dead Na exhibit a strong preferred orientation in the (200) crystallographic plane, indicating that the overall texture of Na metal does not change appreciably after stripping. This stable (200) texture reflects the dominance of bulk Na domains that persist through the cycle. In contrast, NaH shows a markedly different evolution: it initially forms with a preferred (111) orientation during deposition but shifts toward a dominant (200) orientation after stripping. This difference suggests that while the bulk Na framework remains texturally stable, NaH forms and reforms primarily within the dynamic interfacial regions where dissolution, renucleation, and local chemical environments vary during cycling. Thus, NaH orientation is more sensitive to interfacial processes, whereas the Na metal texture reflects the more stable bulk Na that remains throughout the cycle.

To better understand how the SEI forms and evolves in sodium batteries, it is essential to characterize its chemical composition in detail. In addition to the inorganic components discussed above, it is important to recognize that the SEI on sodium metal is composed of inorganic and organic components.[21] Inorganic species such as NaF and Na_2O are typically crystalline, whereas organic compounds (e.g., $ROCO_2Na$) and Na_2CO_3 are generally amorphous.[20,33] Understanding the distribution and chemical nature of these species is essential for elucidating SEI formation and evolution.

While X-ray photoelectron spectroscopy (XPS) is a widely used technique for analyzing SEI chemistry, obtaining depth profiles typically requires ion sputtering.[34] To complement such approaches, we employed soft X-ray absorption spectroscopy (sXAS), which enables nondestructive, depth-sensitive analysis. By collecting signals in partial electron yield (PEY) and total electron yield (TEY) modes, sXAS can probe the outer (approximately 5 nm) and inner (approximately 10 nm) SEI layers, respectively, providing detailed insight into the spatial distribution of inorganic and organic species.

Figure 3(A) presents Na K-edge spectra collected in TEY mode during the first cycle, representing typical inorganic SEI components. Figures S13 and S14 show complementary Na K-edge spectra acquired in both TEY and PEY modes under various cycling conditions, including the first and 30th cycles. To determine the relative proportions of possible compounds in SEI, linear combination fitting of the Na K-edge spectra was performed in both modes (Figures S15 and S16). Figure 3(B) presents the depth-resolved composition of SEI components under various cycling conditions, including both deposition and stripping during the first and 30th cycles. The electrochemical performance data voltage profile and its Coulombic efficiency corresponding to these cycling protocols are shown in Figure S17.

Na_2O is consistently the dominant inorganic phase in both the outer and inner SEI layers, regardless of whether the electrode is in the deposition or stripping state.[10] This is consistent with the O K-edge data, as seen in Figure S18A. In terms of NaF, it forms in the outer layer of SEI during deposition but disappears after stripping, suggesting it is either dissolved or mechanically detached. A similar trend is observed in the F K-edge spectra shown in Figure S18B, highlighting the transient nature of SEI. NaF is widely considered beneficial in the SEI due to its chemical stability, mechanical robustness, ionic conductivity, and its ability to form a passivating layer that suppresses side reactions and inhibits dendritic growth.[35] The disappearance of NaF after stripping suggests the instability of SEI in the 1 mol/L $NaPF_6$ diglyme electrolyte, consistent with previous *operando* GIWAXS observation. As cycling continues, additional inorganic components such as NaOH, NaH, and Na_2CO_3 appear, indicating increasing SEI chemical complexity within the SEI.

Building on the understanding of inorganic phases, we next examine the contribution of organic species to the evolving SEI composition. Figure 3 (C) and Figure S19 present C K-edge spectra with peak assignments corresponding to key functional groups: C═C (284.9 eV), C═O (288.6 eV), C−H (290.2 eV), and C−C (292.4 eV).[36,37] C═C/C−C and C═O/C−H ratios derived from carbon K-edge spectra provide valuable

https://doi.org/10.1021/acsenergylett.5c03538
ACS Energy Lett. 2026, 11, 3181−3189

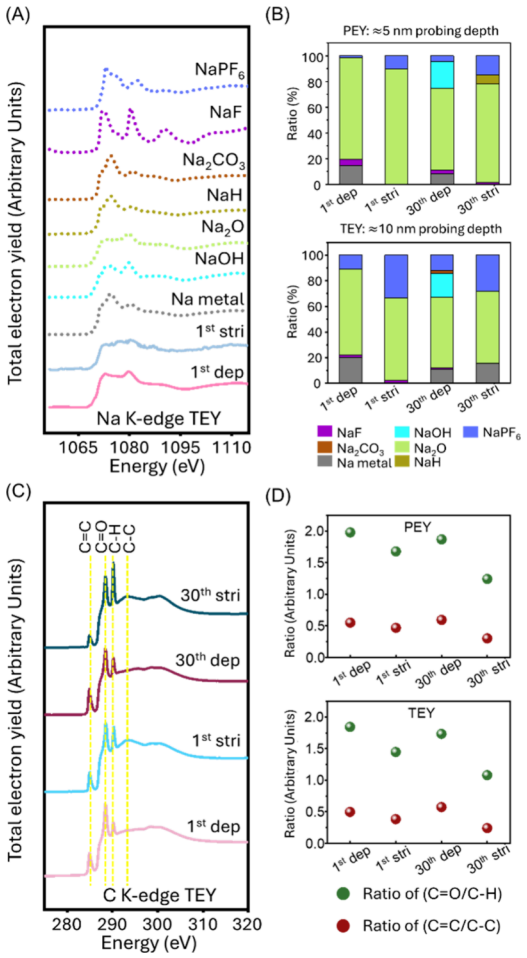

Figure 3. Depth-resolved analysis of inorganic and organic SEI composition using sXAS for different cycling conditions. (A) Na K-edge spectra collected in TEY mode, representing the inner layer of the SEI. The powder standards, $NaPF_6$, Na_2CO_3, NaH, Na_2O, NaOH and NaF are shown in dashed lines. (B) Relative composition of inorganic SEI species extracted from Na K-edge spectra through linear combination fitting under various cycling conditions. (C) Carbon K-edge spectra collected in TEY mode. (D) Evolution of sp^2/sp^3 (C═C/C−C) and carbonyl/hydrocarbon (C═O/C−H) ratios, used as qualitative indicators of SEI electronic character and oxidation state under varying electrochemical conditions. In the figure, stripped samples are labeled as "stri" and deposited samples are labeled as "dep".

insight into the chemical evolution of the organic components within the SEI. The C═C/C−C ratio reflects the relative abundance of sp^2- versus sp^3-hybridized carbon, serving as a qualitative indicator of the electronic structure of SEI.[38] A higher C═C/C−C ratio suggests a greater presence of unsaturated, graphitic, or conjugated species, which are typically more electronically conductive, while a lower C═C/C−C ratio indicates a dominance of saturated, aliphatic, and polymeric components associated with a more insulating and degraded SEI. Additionally, C═O/C−H ratio tracks the oxidation state and functional group composition of the SEI. An elevated ratio points to increased carbonyl or carbonate content, often correlated with more polar, rigid, and passivating organic species. Conversely, a lower C═O/C−H ratio reflects a SEI rich in hydrocarbon-like chains, which are less oxidized and may contribute to reduced structural integrity or passivation efficiency.[26] Together, quantifying the ratios of these different types of bonding offers a chemically resolved, depth-sensitive picture of SEI formation and degradation, helping to interpret its protective properties and long-term stability under different cycling conditions.

Figure 3(D) shows these indicators across different cycling stages and outer and inner SEI have the same trend. The ratio of sp^2/sp^3 (C═C/C−C ratio) remains relatively unchanged after the first deposition and stripping but declines with extended cycling, which implies that SEI becomes more insulating after long cycling. The ratio of carbonyl/hydrocarbon (C═O/C−H ratio) is consistently greater during deposition than stripping and gradually reduces over time, suggesting the SEI becomes less compact and possibly less protective with prolonged cycling.

The electrochemical impedance spectroscopy (EIS) measurements and the corresponding voltage profile are as demonstrated in Figure S20. Initially, the significant resistance in the resting step indicates unplated Cu and possibly incompletely wetted interfaces. After the first plating half-cycle, the resistance dropped to ≈10 Ω, indicating successful cell activation, and the EIS curve showed two semicircles. The lower-frequency one is most likely corresponding to the still-forming SEI and species related to surface passivation. In the EIS after the second plating, the semicircles merged into a single semicircle, indicating a more complete and uniform SEI structure.

On the other hand, the EIS of the samples after the stripping process all displays two semicircles and larger resistance. The higher resistance is most likely due to the stripping of Na metal, exposing the less conductive SEI. The re-emergence of two semicircles is likely due to the same process. As Na strips, the more heterogeneous SEI layer is exposed and may be morphologically affected, resulting in multiple interfaces in EIS measurements and increased resistance. This R fluctuation is repeatable. Overall, the EIS results are consistent with our other characterization data and further support our interpretation of the SEI evolution.

We next develop a mesoscale modeling framework to investigate how heterogeneity and the distribution of different SEI components influence electrodeposition stability at the Na metal anode interface.[39] Figure 4(A) shows a schematic representation of the system considered in the model, consisting of electrolyte, Na and SEI. The schematic highlights the heterogeneous nature of the SEI, where multiple components with distinct transport properties can alter ionic conduction pathways. It was earlier shown that multiple SEI components, such as NaF, NaH, Na_2O, Na_2CO_3, and NaOH, emerge during cycling. These phases exhibit distinct ionic transport properties and such compositional differences can strongly influence current distribution and stability. Alkali metal fluorides, for example, are known to exhibit relatively higher ionic conductivity and tend to form a more compact and uniform SEI.[10,40,41] On the other hand, relatively resistive phases such as Na_2CO_3 and NaOH,[20,33] which accumulate after extended cycling, may enhance current heterogeneity. Moreover, the preferred crystallographic orientation of SEI phases, as observed in *operando* GIWAXS, can further modulate their transport properties. The components aligned along favorable directions may provide relatively easier ionic pathways, whereas misaligned orientations can act as transport bottlenecks, amplifying nonuniformity at the interface. A low-conductivity SEI promotes current focusing in low-resistance or thinner SEI regions, as shown in Figure 4(B), whereas a

https://doi.org/10.1021/acsenergylett.5c03538
ACS Energy Lett. 2026, 11, 3181−3189

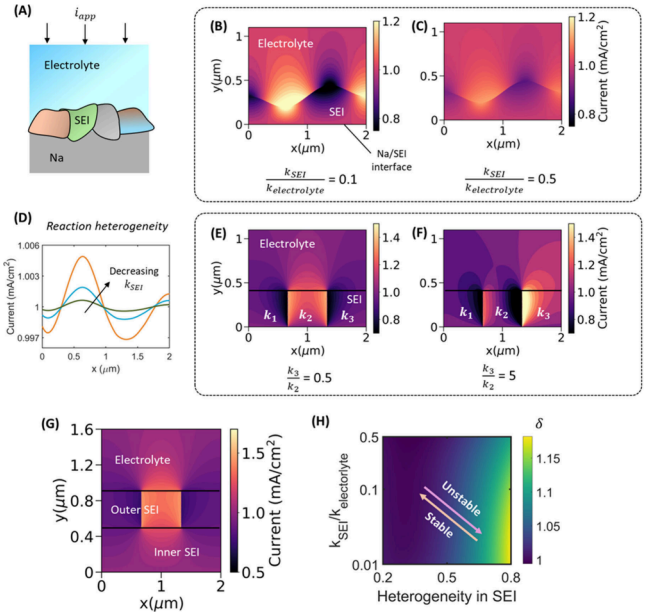

Figure 4. Mesoscale modeling showing how heterogeneity and the distribution of different SEI components influence electrodeposition stability at the Na metal anode interface: (A) Schematic illustration of the model domain consisting of Na, electrolyte and SEI. (B, C) Current distribution for different values of SEI ionic conductivity, given by $k_{SEI}/k_{electrolyte}$, for i_{app} = 1 $mA\ cm^{-2}$. (D) Reaction current density at the Na/SEI interface for different k_{SEI}. (E, F) Effect of spatial heterogeneity in the SEI on the current distribution profile (k_1/k_2 = 0.5 for both cases). (G) Current distribution for both inner and outer SEI ($k_{inner}/k_{electrolyte}$ = 0.1,k_3/k_2 = 0.5, k_3 = k_1). (H) Phase map showing the combined influence of SEI heterogeneity and conductivity on interface instability, given by $\delta = i_{max}/i_{min}$.

higher SEI conductivity leads to a more uniform current distribution, shown in Figure 4(C). The impact of SEI conductivity on the reaction current density is shown in Figure 4(D), and decreasing ionic conductivity amplifies reaction heterogeneity at Na/SEI interface. Nonuniform electrodeposition across such a heterogeneous SEI leads to stress accumulation (Figure S21), promoting morphological instability and eventual SEI failure.

Figure 4(E,F) illustrates how spatial heterogeneity in component distribution (e.g., NaF, Na_2CO_3, NaOH) alters the current profile. Here, the spatial heterogeneity in the SEI is given by ratio of the ionic conductivity of different components, k_1, k_2 and k_3. Current focusing occurs in regions with relatively higher conductivity, while adjacent resistive regions redirect flux, producing sharp gradients. These trends are particularly relevant during extended cycling, where Na_2O detected in early cycles evolves into a mixed SEI composition containing Na_2CO_3 and NaOH, as indicated by sXAS (Figure 3). Figure 4(G) shows the current profile with both outer SEI (multiple components) and inner/interior SEI (assumed single component for clarity). Figure S22 compares cases with different spatial heterogeneity in the outer SEI, while Figure S23 illustrates the potential distribution as a function of the ionic conductivity of the inner SEI ($k_{inner}/k_{electrolyte}$). Together, these results highlight that both the intrinsic properties and the spatial distribution of SEI components, across outer and inner layers, critically dictate electrodeposition stability.

Finally, Figure 4(H) quantifies the combined effect of heterogeneity and conductivity of the SEI. Here, the heterogeneity in SEI is defined as the nonuniformity in SEI morphology and is given by L_d/L_{ref}, where L_d is the difference between the maximum and minimum SEI thickness and L_{ref} is a constant reference length proportional to SEI thickness. The instability descriptor δ quantifies the reaction heterogeneity and is defined as $\delta = i_{max}/i_{min}$, where i_{max} and i_{min} are the maximum and minimum reaction current density. A higher morphological heterogeneity, together with lower component ionic conductivity, results in more unstable deposition. Conversely, a spatially uniform, high-conductivity SEI promotes more homogeneous electrodeposition. Overall, these results suggest that the evolving composition of the SEI plays a key role in dictating interface instability and growth.

In summary, using synchrotron *operando* GIWAXS and sXAS analysis, this work shows SEI undergoes spatially and temporally heterogeneous formation and dissolution of inorganic and organic phases, with NaF and NaH appearing early and consistently, and Na_2PO_3F forming later via salt decomposition. Mesoscale modeling connects these evolving SEI structures and heterogeneity to localized current density fluctuations, which trigger interfacial instabilities leading to partial loss of passivation and the onset of dendrite formation. This integrated experimental and modeling approach clarifies how compositional and structural inhomogeneity and dynamic reactions could drive sodium metal degradation, providing a mechanistic foundation for designing more robust, reversible Na metal anodes. Looking ahead, understanding the persistence, reversibility, and longer-term degradation pathways of SEI phases will be essential for advancing stable Na metal batteries. Extending *operando* and multimodal characterization methods to long-term cycling represents an important direction for future studies.

■ ASSOCIATED CONTENT

Supporting Information

The Supporting Information is available free of charge at https://pubs.acs.org/doi/10.1021/acsenergylett.5c03538.

Experimental details, electrochemical modeling details, *operando* GIWAXS analysis of Na plating/stripping, absorption spectra, linear combination fitting result, and voltage profiles (PDF)

■ AUTHOR INFORMATION

Corresponding Authors

Partha P. Mukherjee − *School of Mechanical Engineering, Purdue University, West Lafayette, Indiana 47907, United States*; Email: mukher28@purdue.edu

Yu-chen Karen Chen-Wiegart − *Department of Materials Science and Chemical Engineering, Stony Brook University, Stony Brook, New York 11794, United States; National Synchrotron Light Source II, Brookhaven National Laboratory, Upton, New York 11973, United States;* orcid.org/0000-0003-4445-2159; Email: Karen.Chen-Wiegart@stonybrook.edu

Authors

Chang-An Lo − *Department of Materials Science and Chemical Engineering, Stony Brook University, Stony Brook, New York 11794, United States;* orcid.org/0009-0006-7271-3028

https://doi.org/10.1021/acsenergylett.5c03538
ACS Energy Lett. 2026, 11, 3181−3189

Aditya Singla − *School of Mechanical Engineering, Purdue University, West Lafayette, Indiana 47907, United States*
Varun R. Kankanallu − *Department of Materials Science and Chemical Engineering, Stony Brook University, Stony Brook, New York 11794, United States;* orcid.org/0000-0002-0954-5803
Dean Yen − *Department of Materials Science and Chemical Engineering, Stony Brook University, Stony Brook, New York 11794, United States*
Bairav S. Vishnugopi − *School of Mechanical Engineering, Purdue University, West Lafayette, Indiana 47907, United States;* orcid.org/0009-0002-6357-9358
Eliot Gann − *National Synchrotron Light Source II, Brookhaven National Laboratory, Upton, New York 11973, United States*
Lutz Wiegart − *National Synchrotron Light Source II, Brookhaven National Laboratory, Upton, New York 11973, United States;* orcid.org/0000-0003-4417-8479
Cherno Jaye − *Material Measurement Laboratory, National Institute of Standards and Technology, Gaithersburg, Maryland 20899, United States*
Patryk Wąsik − *National Synchrotron Light Source II, Brookhaven National Laboratory, Upton, New York 11973, United States*

Complete contact information is available at: https://pubs.acs.org/10.1021/acsenergylett.5c03538

Notes

The authors declare no competing financial interest.

■ ACKNOWLEDGMENTS

We gratefully acknowledge support from the U.S. Department of Energy, Office of Science, Basic Energy Sciences under Award# DE-SC0023260. This research used the Soft Matter Interfaces beamline (SMI, 12-ID) and the Spectroscopy Soft and Tender beamline (SST-1, 7-ID-1) of the National Synchrotron Light Source II, a U.S. Department of Energy (DOE) Office of Science by Brookhaven National Laboratory under Contract No. DESC0012704. We thank Jason Visentin and James Eksi of the Physics Machine Shop of Stony Brook University and Michael Maklary of Brookhaven National Laboratory for their technical support in *operando* GIWAXS electrochemical cells. Commercial equipment, instruments, materials, suppliers, or software are identified in this paper for illustrative purposes. Such identification does not imply recommendation or endorsement by the National Institute of Standards and Technology, nor does it imply that the materials or equipment identified are necessarily the best available for the purpose.

■ REFERENCES

(1) Islam, S.; Weerasinghe, H.; Prado, D. M.; Gonzaga, A. N.; Burda, C. Diversifying the Materials and Technologies for the Future of Energy Storage. *Energy Fuels* **2025**, *39* (18), 8369−8390.
(2) Tabelin, C. B.; Dallas, J.; Casanova, S.; Pelech, T.; Bournival, G.; Saydam, S.; Canbulat, I. Towards a low-carbon society: A review of lithium resource availability, challenges and innovations in mining, extraction and recycling, and future perspectives. *Minerals Engineering* **2021**, *163*, 106743.
(3) Li, H.; Wu, F.; Wang, J.; Wang, J.; Qu, H.; Chen, M.; Zhang, H.; Passerini, S. Anode-free sodium metal batteries: optimization of electrolytes and interphases. *Energy Environ. Sci.* **2025**, *18* (9), 3887−3916.
(4) Huang, J.; Wu, K.; Xu, G.; Wu, M.; Dou, S.; Wu, C. Recent progress and strategic perspectives of inorganic solid electrolytes: fundamentals, modifications, and applications in sodium metal batteries. *Chem. Soc. Rev.* **2023**, *52* (15), 4933−4995.
(5) Huang, F.; Xu, P.; Fang, G.; Liang, S. In-depth understanding of interfacial Na+ behaviors in sodium metal anode: migration, desolvation, and deposition. *Adv. Mater.* **2024**, *36* (41), 2405310.
(6) Hu, Z.; Liu, L.; Wang, X.; Zheng, Q.; Han, C.; Li, W. Current progress of anode-free rechargeable sodium metal batteries: origin, challenges, strategies, and perspectives. *Adv. Funct. Mater.* **2024**, *34* (22), 2313823.
(7) Zheng, J.; Chen, S.; Zhao, W.; Song, J.; Engelhard, M. H.; Zhang, J.-G. Extremely stable sodium metal batteries enabled by localized high-concentration electrolytes. *ACS Energy Letters* **2018**, *3* (2), 315−321.
(8) Chen, J.; Peng, Y.; Yin, Y.; Liu, M.; Fang, Z.; Xie, Y.; Chen, B.; Cao, Y.; Xing, L.; Huang, J.; et al. High energy density Na-metal batteries enabled by a tailored carbonate-based electrolyte. *Energy Environ. Sci.* **2022**, *15* (8), 3360−3368.
(9) Cheng, Z.; Zhang, Z.; Qiu, F.; Gao, Z.; Xie, H.; Xu, Z.; Jia, M.; Zhang, X.; Zhou, H. Regulating solvation shell to fortify anion-cation coordination for enhanced sodium metal battery stability. *ACS Energy Letters* **2025**, *10* (1), 177−184.
(10) Seh, Z. W.; Sun, J.; Sun, Y.; Cui, Y. A highly reversible room-temperature sodium metal anode. *ACS central science* **2015**, *1* (8), 449−455.
(11) Yi, Q.; Lu, Y.; Sun, X.; Zhang, H.; Yu, H.; Sun, C. Fluorinated ether based electrolyte enabling sodium-metal batteries with exceptional cycling stability. *ACS Appl. Mater. Interfaces* **2019**, *11* (50), 46965−46972.
(12) Sarkar, S.; Lefler, M. J.; Vishnugopi, B. S.; Nuwayhid, R. B.; Love, C. T.; Carter, R.; Mukherjee, P. P. Fluorinated ethylene carbonate as additive to glyme electrolytes for robust sodium solid electrolyte interface. *Cell Reports Physical Science* **2023**, *4* (4), 101356.
(13) Gao, Y.; Yao, Y.; Shi, P.; Huang, F.; Jiang, Y.; Yu, Y. Advanced Interphases Layers for Dendrite-Free Sodium Metal Anodes. *ACS Appl. Mater. Interfaces* **2025**, *17* (12), 17881−17894.
(14) Wang, Y.; Dong, H.; Katyal, N.; Vishnugopi, B. S.; Singh, M. K.; Hao, H.; Liu, Y.; Liu, P.; Mukherjee, P. P.; Henkelman, G.; et al. Intermetallics based on sodium chalcogenides promote stable electrodeposition-electrodissolution of sodium metal anodes. *Adv. Energy Mater.* **2023**, *13* (27), 2204402.
(15) Lv, S.; Verhallen, T.; Vasileiadis, A.; Ooms, F.; Xu, Y.; Li, Z.; Li, Z.; Wagemaker, M. Operando monitoring the lithium spatial distribution of lithium metal anodes. *Nat. Commun.* **2018**, *9* (1), 2152.
(16) Seok, J.; Hyun, J.-H.; Jin, A.; Um, J. H.; Abruna, H. D.; Yu, S.-H. Visualization of sodium metal anodes via operando X-ray and optical microscopy: controlling the morphological evolution of sodium metal plating. *ACS Appl. Mater. Interfaces* **2022**, *14* (8), 10438−10446.
(17) Zheng, B.; Liu, X.; Xiang, Y. Solid-State Nuclear Magnetic Resonance Studies of Lithium and Sodium Metal Batteries. *J. Phys. Chem. C* **2024**, *128* (44), 18659−18677.
(18) Xiang, Y.; Zheng, G.; Liang, Z.; Jin, Y.; Liu, X.; Chen, S.; Zhou, K.; Zhu, J.; Lin, M.; He, H.; et al. Visualizing the growth process of sodium microstructures in sodium batteries by in-situ 23Na MRI and NMR spectroscopy. *Nature Nanotechnol.* **2020**, *15* (10), 883−890.
(19) Ji, Y.; Qiu, J.; Zhao, W.; Liu, T.; Dong, Z.; Yang, K.; Zheng, G.; Qian, G.; Yang, M.; Chen, Q.; et al. In situ probing the origin of interfacial instability of Na metal anode. *Chem.* **2023**, *9* (10), 2943−2955.
(20) Han, B.; Zou, Y.; Zhang, Z.; Yang, X.; Shi, X.; Meng, H.; Wang, H.; Xu, K.; Deng, Y.; Gu, M. Probing the Na metal solid electrolyte interphase via cryo-transmission electron microscopy. *Nat. Commun.* **2021**, *12* (1), 3066.
(21) Lee, B.; Paek, E.; Mitlin, D.; Lee, S. W. Sodium metal anodes: emerging solutions to dendrite growth. *Chem. Rev.* **2019**, *119* (8), 5416−5460.

(22) Lo, C. A.; Wang, Y.; Kankanallu, V. R.; Singla, A.; Yen, D.; Zheng, X.; Naik, K. G.; Vishnugopi, B. S.; Campbell, C.; Raj, V.; et al. Interdependence of Support Wettability-Electrodeposition Rate-Sodium Metal Anode and SEI Microstructure. *Angew. Chem.* **2025**, *137* (8), No. e202412550.
(23) Bao, C.; Wang, B.; Liu, P.; Wu, H.; Zhou, Y.; Wang, D.; Liu, H.; Dou, S. Solid electrolyte interphases on sodium metal anodes. *Adv. Funct. Mater.* **2020**, *30* (52), 2004891.
(24) Monroe, C.; Newman, J. The impact of elastic deformation on deposition kinetics at lithium/polymer interfaces. *J. Electrochem. Soc.* **2005**, *152* (2), A396.
(25) Kim, J.; Kim, J.; Jeong, J.; Park, J.; Park, C.-Y.; Park, S.; Lim, S. G.; Lee, K. T.; Choi, N.-S.; Byon, H. R.; et al. Designing fluorine-free electrolytes for stable sodium metal anodes and high-power seawater batteries via SEI reconstruction. *Energy Environ. Sci.* **2022**, *15* (10), 4109−4118.
(26) Wang, X.; Lu, J.; Wu, Y.; Zheng, W.; Zhang, H.; Bai, T.; Liu, H.; Li, D.; Ci, L. Building stable anodes for high-rate Na-metal batteries. *Adv. Mater.* **2024**, *36* (16), 2311256.
(27) Iermakova, D.; Dugas, R.; Palacín, M.; Ponrouch, A. On the comparative stability of Li and Na metal anode interfaces in conventional alkyl carbonate electrolytes. *J. Electrochem. Soc.* **2015**, *162* (13), A7060.
(28) Singla, A.; Naik, K. G.; Vishnugopi, B. S.; Mukherjee, P. P. Chemo-Mechanics Interplay Dictates Interface Instability and Asymmetry in Plating and Stripping of Sodium Metal Electrodes. *Adv. Funct. Mater.* **2025**, *35*, 2418033.
(29) Wang, Y.; Yang, X.; Meng, Y.; Wen, Z.; Han, R.; Hu, X.; Sun, B.; Kang, F.; Li, B.; Zhou, D.; et al. Fluorine chemistry in rechargeable batteries: Challenges, progress, and perspectives. *Chem. Rev.* **2024**, *124* (6), 3494−3589.
(30) Wang, Y.; Wu, Z.; Azad, F. M.; Zhu, Y.; Wang, L.; Hawker, C. J.; Whittaker, A. K.; Forsyth, M.; Zhang, C. Fluorination in advanced battery design. *Nature Reviews Materials* **2024**, *9* (2), 119−133.
(31) Smith, T. *Characterising Electrolyte Interactions with Carbon Anodes for Sodium Ion Batteries*. Thesis; University of Cambridge: 2022. DOI: 10.17863/CAM.86259
(32) Qin, B.; Ma, Y.; Li, C.; Xu, H.; Li, J.; Xie, B.; Du, X.; Dong, S.; Xu, G.; Cui, G. Sodium hydride inspired the clarification of the ether-carbonate solvent disparity in sodium metal anodes. *Energy Storage Materials* **2023**, *61*, 102891.
(33) Sayahpour, B.; Li, W.; Bai, S.; Lu, B.; Han, B.; Chen, Y.-T.; Deysher, G.; Parab, S.; Ridley, P.; Raghavendran, G.; et al. Quantitative analysis of sodium metal deposition and interphase in Na metal batteries. *Energy Environ. Sci.* **2024**, *17* (3), 1216−1228.
(34) Lee, J.; Kim, J.; Kim, S.; Jo, C.; Lee, J. A review on recent approaches for designing the SEI layer on sodium metal anodes. *Materials Advances* **2020**, *1* (9), 3143−3166.
(35) Zhu, C.; Wu, D.; Wang, Z.; Wang, H.; Liu, J.; Guo, K.; Liu, Q.; Ma, J. Optimizing NaF-rich solid electrolyte interphase for stabilizing sodium metal batteries by electrolyte additive. *Adv. Funct. Mater.* **2024**, *34* (5), 2214195.
(36) Heymann, K.; Lehmann, J.; Solomon, D.; Schmidt, M. W.; Regier, T. C 1s K-edge near edge X-ray absorption fine structure (NEXAFS) spectroscopy for characterizing functional group chemistry of black carbon. *Org. Geochem.* **2011**, *42* (9), 1055−1064.
(37) Baio, J. E.; Jaye, C.; Sullivan, E.; Rasmussen, M. H.; Fischer, D. A.; Gorb, S.; Weidner, T. NEXAFS imaging to characterize the physio-chemical composition of cuticle from African Flower Scarab Eudicella gralli. *Nat. Commun.* **2019**, *10* (1), 4758.
(38) Liu, W.; Liu, P.; Mitlin, D. Review of emerging concepts in SEI analysis and artificial SEI membranes for lithium, sodium, and potassium metal battery anodes. *Adv. Energy Mater.* **2020**, *10* (43), 2002297.
(39) Singla, A.; Naik, K. G.; Vishnugopi, B. S.; Mukherjee, P. P. Heterogeneous solid electrolyte interphase interactions dictate interface instability in sodium metal electrodes. *Advanced Science* **2024**, *11* (36), 2404887.
(40) Gong, C.; Pu, S. D.; Gao, X.; Yang, S.; Liu, J.; Ning, Z.; Rees, G. J.; Capone, I.; Pi, L.; Liu, B.; et al. Revealing the role of fluoride-rich battery electrode interphases by operando transmission electron microscopy. *Adv. Energy Mater.* **2021**, *11* (10), 2003118.
(41) Guo, R.; Gallant, B. M. Li2O solid electrolyte interphase: probing transport properties at the chemical potential of lithium. *Chem. Mater.* **2020**, *32* (13), 5525−5533.

https://doi.org/10.1021/acsenergylett.5c03538
ACS Energy Lett. 2026, 11, 3181−3189